Catalysis Communications 171 (2022) 106527

Contents lists available at ScienceDirect

Catalysis Communications

journal homepage: www.elsevier.com/locate/catcom

Zn-doped titania nanoparticles as building blocks for solid foam filters of water and air via photocatalytic oxidation

M. Vaccari [a], M. Cremona [a], D. Orsi [a], V. Lorusso [a], A. Baraldi [a], A. Bosio [a], D. Pontiroli [a], L. Liggieri [b], F. Ravera [b], E. Santini [b], L. Cristofolini [a,b,*]

[a] Department of Mathematical Physical and Computer Sciences, University of Parma, Parma, Italy
[b] Institute of Condensed Matter Chemistry and Technologies for Energy – CNR, Department of Genova, Italy

ARTICLE INFO

Keywords:
Photocatalytic oxidation (PCO)
Titania nanoparticles
Air purification
Water purification
Porous materials
Solid foams

ABSTRACT

Photocatalytic oxidation (PCO) could provide energy-efficient purification of water and air. Its efficacy is constrained mainly by limited photocatalytic activity and active surface. To address both, solid foams with hierarchic porous structures spanning multiple length-scales, stabilized by photocatalytic Zn-doped titania nanoparticles (NP) were synthesized and tested. The NP were characterized by SEM, EDS, DLS, XRD, Raman and UV–Vis spectroscopies. Solid foams were stabilized by NP complexes with cationic surfactants. The foam morphology was characterized and photocatalytic activity was demonstrated in water. The present work paves the way for the development of efficient systems for air and water purification in demanding technological sectors, such as aerospace.

1. Introduction

Energy efficient air and water purification means are always needed, and even more in the present scenario of uncertainty in the energy supply. For instance, air purification is required to lower or eliminate unwanted atmospheric components, such as particulate, volatile organic compounds (VOC) and microorganisms (either viruses, such as SARS-COV-2, bacteria, or fungi). A universal solution is not available, but photocatalytic oxidation (PCO) is emerging as an energy-effective technology with the potential to treat simultaneously VOCs and microorganisms. However, a technical summary issued in 2018 by the United States Environmental Protection Agency [1] states that "There are few field investigations to validate the performance of PCO air cleaners, and laboratory studies demonstrate high variability and often relatively low removal efficiency for many common indoor gases…The report indicated that the PCO devices studied might not work as advertised." Further, "The usefulness of PCO air cleaners depends on the amount of catalyst, the amount of contact time between gaseous pollutants and the catalyst, and the amount of UV-light that is delivered to the catalyst surface. If any one of these factors is not addressed in the design of the device, a PCO air cleaner may fail to destroy pollutants completely, and instead produce new indoor pollutants including irritants."

Classically, PCO devices are based on anatase titania (TiO_2) in the form of nanocrystals or film, activated by UV-C light. UV-C radiation itself provides some activity against microorganisms, often also causing production of ozone, which requires a further downstream filtration to avoid its irritating effects. More recently, PCO activated by visible light has been proposed, employing more efficient LED sources and with longer operational life than the Hg lamps employed in classical PCO filters [2]. Besides, avoiding UV ensures ozone-free operation.

Titania has four natural polymorphs: rutile, anatase, akaogiite and brookite. Rutile and anatase are the more common ones; rutile is the thermodynamically stable polymorph. Consequently, the other polymorphs would eventually convert into rutile upon some thermal treatment. Since it is the anatase crystal structure to be associated with the highest photocatalytic efficiency [3,4], it is important to check the crystalline form of the titania intended to be employed for PCO applications. This is best done via a combination of powder X-ray diffraction and Raman scattering spectroscopies. The high sensitivity of the latter to the anatase polymorph might lead to an overestimation of the anatase in the solid if only Raman spectroscopy was used as diagnostic tool.

Titania nanoparticles (NP) can be synthesized by two fundamentally different approaches: *top-down* or *bottom-up*. While the former starts with bulk material and employs various techniques to finally obtain the desired particle size distribution, the latter uses chemical synthesis methods starting from appropriate molecular precursors as in the case of

* Corresponding author at: Department of Mathematical Physical and Computer Sciences, University of Parma, Parma, Italy.
E-mail address: luigi.cristofolini@unipr.it (L. Cristofolini).

https://doi.org/10.1016/j.catcom.2022.106527
Received 24 June 2022; Received in revised form 3 October 2022; Accepted 6 October 2022
Available online 7 October 2022

sol-gel synthesis of titania nanoparticles. This route is particularly attractive because it yields anatase, either pure or as majority phase [5]. In the quest for PCO activated by visible light, early attempts to produce titania NPs with reduced bandgap by employing organic dyes proved unsuccessful, yielding unstable complexes. On the contrary, inclusion of metal ions was found to provide stable NPs with reduced bandgap energy, allowing PCO excited by visible light [4,6,7]. Further, oxidative stress induced by metal ion-doped titania was investigated also in human cells [8]. Promising for the purposes of the present work, it was found that moderate Zn doping (around 0.5 %molar ratio Zn/Ti) slightly reduces the band gap energy while maintaining the high photocatalytic activity, typical of pure titania [6,7], and stabilizes anatase phase, thus hindering the thermally induced phase transition from anatase to rutile [9,10]. On these grounds, we propose a way to create efficient photocatalytic filters by creating three-dimensional structures with high interfacial density and percolating pores, obtained as solid foams containing these photocatalytic titania NPs.

Solid foams with open cell structure, high specific surface area and hierarchical porosity are used in many applications nowadays, like gas adsorption, filtering and catalysis [11]. Their fabrication by solidification of particle-stabilized foams, also referred as direct foaming methods [12] provides tailored features and specific composition of the final product. These methods, mainly developed for macro-porous ceramics [13–15], have been also applied to meso-porous alumina, silica and carbon-based materials [16–19]. The amphiphilicity of the complexes formed by water dispersed hydrophilic nanoparticles and appropriate surfactants can be optimized by tuning the ratio between surfactant and NP content [20]. Such complexes can be used to stabilize liquid foams. Subsequently, the foams can be solidified by gel-casting, employing a polymer (as polyvinyl alcohol, PVA) and a cross-linking agent (as dimethoxy-dihydrofuran, DHF). Jellying time can be controlled by the concentration of cross-linking agent, pH or temperature [21]. A mild heat treatment yields a solid foam whose structure contains and is stabilized by the NPs.

2. Materials and methods

2.1. Synthesis of Zn-doped TiO_2

We exploited a well-documented strategy to produce Zn- doped titania NPs, a sol-gel synthesis process in isopropanol in the presence of Ti and Zn precursors, followed by calcination at 500 ° C [6]. This is represented schematically in panel A) of Fig. 1 (Section 3.1). During the synthesis, a hydroalcoholic solution was added dropwise to an alcoholic solution containing the titania precursor. For the realization of the titania precursor's solution, 17 mL of titanium (IV) butoxide ($Ti(OBu)_4$) were dissolved in 40 mL of isopropyl alcohol; the *pH* of the solution was adjusted to 3 by adding hydrochloric acid (HCl). Subsequently, a variable amount of zinc nitrate hexahydrate ($Zn(NO_3)_2 \bullet 6H_2O$) was dissolved in 3.6 mL of ultrapure water from a MilliQ-Millirho purification system ($\rho > 18M\Omega \cdot cm$). This zinc nitrate aqueous solution was then mixed with 42 mL of isopropyl alcohol and added dropwise to the titania precursor's solution while stirring at 380 rpm at 25 °C.

Different amounts of zinc nitrate were used to produce the desired

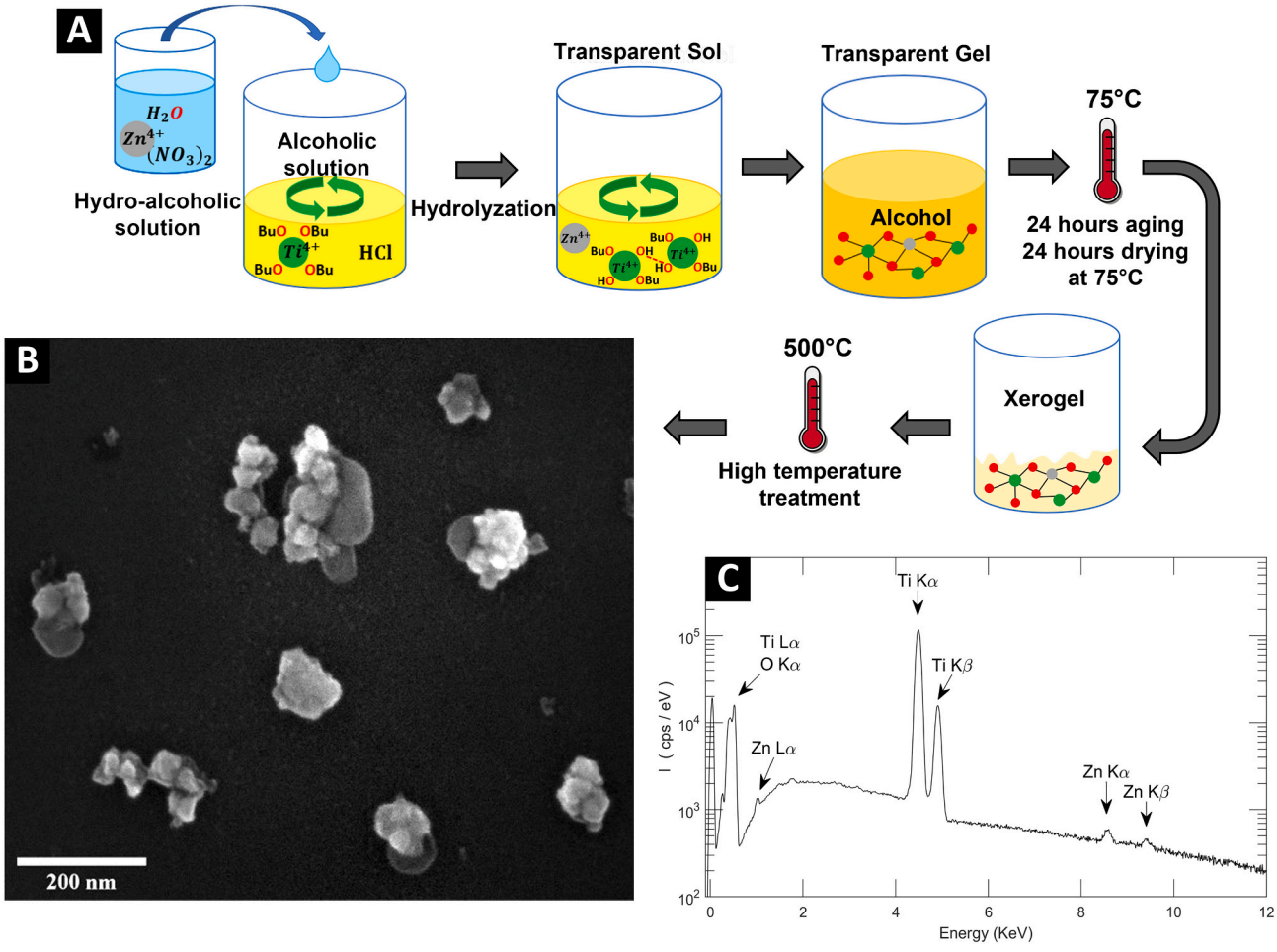

Fig. 1. A) Schematic view of the synthetic route of Zn-doped TiO_2 NPs. B) SEM image of some clusters of 2 mol% Zn -doped titania. C) EDS spectrum of a cluster of TiO_2 nanoparticles with 0.5 mol% nominal Zn content. Labels indicate the emission peaks from Ti, Zn and O.

zinc doping, expressed as Zn/Ti atom fraction. We explored doping in the 0–4 mol% range. After about 1 h from the end of the dripping process, a gel was formed, which was then left at 25 ° C for 12 h by turning off the stirring. The gel was then washed with isopropyl alcohol and dried in a ventilated oven at 80 ° C for 24 h; after the gel-drying step, the solid underwent a calcination heat treatment with maximum temperature of 500 ° C. Titanium (IV) butoxide (reagent grade, 97%), zinc nitrate hexahydrate (reagent grade, 98%) were purchased from Merk, isopropyl alcohol (99%) was purchased from VWR International; all reagents were used without further purification.

2.2. Formation of NP-surfactant complexes and stabilized foams

For the formation of liquid foams, NP-surfactant complexes were obtained by self-assembly, in analogy with past works [18–20], by adding dropwise a water solution of CTAB (Hexadecyltrimethylammonium bromide, 97%, Merck KGaA) to an equal ammount of a water suspension of NPs, while stirring and sonicating to ensure homogeneity. Typically, the final content of NPs was 19 g per 100 g of water, while surfactant content ranged from 1.25 to 125 μmol per gram of NPs.

Foams were generated by a disperser (IKA, Ultraturrax T25N - 18G) operated at 10.000 rpm for 300 s in a 50 mL becker containing 10 mL of suspension. The stability of liquid foams over time has been monitored by automated image acquisition, under standardized conditions, employing a digital camera (The Imaging Source DBK 31BU03) equipped with a fixed focal objective. The image analysis was performed in the Matlab© computing environment. For the formation of solid foams, the liquid fraction has been jellified, according to a gel-casting procedure. In this case, instead of pure water a water solution (80 g/l) of PVA (poly-vinyl-alcohol, 49 kDa, Fluka) was employed to which DHF (2,5-Dimethoxy-2,5-dihydrofuran, 97%, Sigma-Aldrich) was added as a cross linker. The concentrations have been chosen to ensure jellification to occur roughly in 6 min, an optimal time to allow foam generation and preventing major aging effects. After foaming, a mild thermal treatment at 80 ° C for 4 h was applied to harden the gel structure and induce water evaporation.

2.3. Materials characterization by DLS, SEM with EDS, UV–vis, Raman, XRD

Scanning electron microscopy (SEM) micrographs were acquired with a field-emission gun instrument equipped with an in-lens secondary electron detector (Supra40 with GEMINI detector, Zeiss, Germany). A ~20 μL drop of NP suspension in ultrapure water (concentration 10 μg/mL) was placed on a silicon wafer previously cleaned with isopropyl alcohol and dried by keeping it in an oven at 45 ° C for 20 min. Images were acquired with 5 − 10 keV electron beams and have been analyzed with the software ImageJ. Energy Dispersive Spectroscopy (EDS) measurements were performed using a Silicon Drift Detector (SDD, X-act 10 mm^2 LN2-free, Oxford Instruments) mounted on the SEM microscope, under irradiation with 20 keV electrons. Quantitative compositional analysis of EDS spectra was performed using the software Aztec (Oxford Instruments).

To obtain the size distribution of titania NPs, we performed Dynamic Light Scattering (DLS) experiments on aqueous suspensions with a commercial instrument (Brookhaven Instrument Corporation Zetaplus) operating at the wavelength 658 nm, scattering angle 90°, and sample temperature 25 ± 0.1 °C. Correlograms were analyzed by the Brookhaven proprietary software.

UV–vis Diffuse Reflectance Spectroscopy measurements were performed over the 200 – 800 nm range by using a Varian 2390 spectrophotometer equipped with an integrating sphere. For the preparation of the samples used for UV–vis diffuse reflectance measurement, 0.5 g of pure and Zn-doped titania powder were mixed with 0.250 mL of ultrapure water, 0.320 mL of isopropyl alcohol and 0.02 g of vinyl glue. The mixture was deposited on a 2 cm × 2 cm microscope slide and dried in oven at 60 ° C for 1 h, as depicted in panel C of Fig. 2.

Micro-Raman spectra were acquired using a Jobin-Yvon T64000 triple monochromator spectrometer, employing 1800 g/mm gratings. Raman light was collected by a confocal microscope in backscattering depolarized geometry with a 50× objective. Excitation at 473 nm was provided by a power controlled solid state laser, with maximum power to the sample of 1 *mW*. Typical integration times ranged from 5 to 30 s.

Powder X-ray diffraction (XRD) has been performed by a Bruker D8 Discover diffractometer, operating in Debye-Scherrer geometry, equipped with copper anode (Cu − Ka) and a Rayonix MX225 2D area detector. Sample was sealed in a 0.3 mm glass capillary, which was rotated during measurement, to reduce possible effects of preferred orientations on the peak intensity. The powder pattern data were obtained by integrating the collected images (3072 × 3072 pixels) with Fit2D software, after a careful calibration of the experimental setup with a standard (corundum). With the detector at about 11 cm from the sample, the accessible 2θ interval turn out to be in the range $0 - 60°$, sufficient to observe the main peaks of the TiO_2 polymorphs. Quantitative phase analysis has been performed via Rietveld refinement of data, using the GSAS-II suite [22]. We collected diffraction patterns of TiO_2 NPs for different levels of Zn doping and calcination times, namely: pure titania, after 12 h of calcination; 0.5 mol% Zn doped titania, after 12 and 72 h of calcination; 2 mol%Zn doped titania, after 2 and 24 h of calcination, and 4 mol% Zn doped titania, after 2, 12, 24 and 72 h of calcination.

2.4. Photocatalytic activity measurements

Photocatalytic activity of both NPs and solid foams was assessed by measuring the ability of the nanoparticles to degrade the chromophore Rhodamine B in water solution. This procedure, for the NP test follows strictly the one reported in [6], has been extended to the test of solid foams.

Rhodamine B (RhB, CAS 81–88-9) was purchased from Merck and used without further purification. Its molar extinction coefficient at $\lambda = 554$ nm was found to be $\epsilon_{RhB} = 9.8(1) \cdot 10^4$ L $mol^{-1}cm^{-1}$. As the light source, we employed a Lot Oriel 81160 solar simulator powered by an unfiltered Xe lamp, providing a final irradiation power inside the sample of the order of $P_{UV} = 20 - 30$ mW/cm^2 in the photon energy range above 3.0 eV, which is the most relevant for the photocatalysis mechanism.

In the test of NPs, ultrapure water was employed to prepare samples of 4 mL water solution of RhB (250 μM) containing 1 g/L of NPs and irradiated them in a petri dish. Sample temperature was kept constant by means of a thermal bath and the sample was kept under constant mechanical agitation during irradiation. At regular time intervals, 150 μL aliquots of the sample were extracted for the quantification of RhB degradation by UV–vis spectroscopy. For this, the sample was diluted 1 : 10 with ultrapure water, and the NPs were precipitated by centrifugation in Eppendorf ® vials. As a control, we also irradiated and analyzed with the same protocol an analogue water solution of RhB not containing any NPs.

In the test of the solid foam, a flat piece of foam of mass 45.5 mg and thickness 2.5 mm was pre-equilibrated overnight with a RhB water solution (75 μM) to neutralize possible physisorption effects that would contribute to reduce the RhB content in solution. Then, the foam and 3.5 mL of the RhB water solution were placed in a sealed plastic petri slide (Millipore) of thickness 4 mm, corresponding to less than 0.2 optical absorbances in the relevant spectral range, and put under irradiation, while mildly agitated by a laboratory oscillator (Polymax 1040, Heidolph Instruments). At regular time intervals, the sealed petri slide was inserted in the UV–vis spectrometer to quantify RhB degradation.

3. Results and discussion

3.1. Materials morphological characterizations by DLS and SEM with EDS

The titania powder was obtained by the synthetic route schematized in panel A of Fig. 1. Its morphology was investigated by SEM

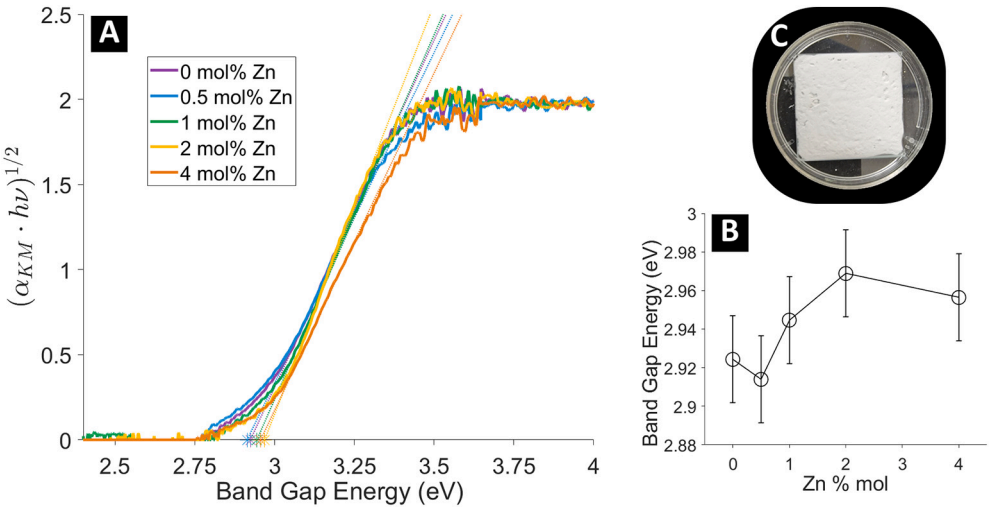

Fig. 2. A) Tauc plot from UV–Vis/DRS measurements. The extrapolation of the band gap energy of pure and *Zn*-doped titania was performed by using the Kubelka-Munk absorption coefficient, α_{KM}. B) Calculated absorption edges as a function of the *Zn* doping molar percentage in titania. C) 4 mol% Zn-doped titania sample annealed for 24 h at 500 °C for UV–Vis/DRS measurements.

microscopy. Panel B reports a typical micrograph where individual isolated particles are observed with size~50 − 100 nm, together with larger NPs clusters. Panel C of Fig. 1 reports an EDS spectrum (20 keV excitation) of a NP cluster of TiO_2 doped with 0.5% Zn/Ti molar ratio. Results of the quantitative EDS analysis are reported in Table 1. They confirm the oxygen stoichiometry and evidences the ratio of atomic contents Zn/Ti is 0.055,in agreement with the nominal composition (5%).

The particle size distribution was better characterized by DLS measurements performed on samples redispersed in water. As supplementary information, we report the size distributions obtained by NNLS algorithm for the same sample investigated by SEM. In this case, most of the particles are non-clustered and have a hydrodynamic diameter of 70 ± 5 nm, however, NPs clusters are also detected, with a size of the order of a few hundreds of nm, in agreement with the qualitative observation by SEM.

3.2. Optical characterization of UV–vis/DRS

UV–vis/DRS spectra $R(\nu)$ have been recorded for NPs of different Zn content and these are reported in Fig. S1 (Supplementary Information, SI). The spectra were analyzed to obtain the corresponding absorption coefficients $\alpha(\nu)$ by the Kubelka-Munk function according to Eq. (1):

$$\alpha_{KM}(\nu) = \frac{(1 - R(\nu))^2}{2R(\nu)} \quad (1)$$

Since anatase titania is a wide-band-gap semiconductor characterized by an indirect allowed gap degenerate with a direct forbidden transition, the absorption edges have been calculated by using the Tauc plot for indirect allowed transition according to the literature [23–25]. The absorption edges are therefore obtained by the linear extrapolations to zero of $(\alpha_{KM} \cdot h\nu)^{1/2}$ as a function of the energy. In panel A of Fig. 2, the Tauc plots for samples with Zn content from 0 to 4 mol% are shown, while in panel B of the same figure the band gaps deduced from the best linear fit are reported. Within experimental uncertainty, which is about 0.02 eV, we find no significant dependence of the band gap energy from the percentage of zinc doping, except perhaps a small decrease for the composition 0.5 mol% followed by an increase for higher Zn content.

Table 1
Results from quantitative EDS analysis of a NPs cluster of *TiO_2/Zn* 0.5 *mol%*; the first column reports the atomic content as a fraction of total, the second column the atomic ratio with respect to titanium.

Element	Atomic content	
	% of total	% with respect to Ti
Ti	33.3(1)	100
O	66.5(3)	200(1)
Zn	0.19(2)	0.55(5)

3.3. Phase purity studied by Raman and X-ray diffraction

To ascertain the crystalline phase of the NPs we resorted to Raman spectrometry. A typical Raman spectrum of TiO_2 doped with 4 mol% Zn and calcined at 500 ° C for 2 h is shown in Fig. 3. Incidentally, we note that samples calcined for less time show a significant fluorescence contribution, presumably due to carbonaceous residues. In the spectrum of Fig. 3, all the observable peaks can be ascribed to the anatase phase of titania, whose position is marked by green vertical bars, while purple vertical bars indicate the position of the Raman peaks of rutile based on the literature. Similar spectra have been recorded for all the samples annealed for less than 72 h. However, it must be recalled that the Raman cross section of rutile is much lower than that of anatase, making hard the detection of minority rutile phases. Therefore, results confirm that most of the sample consists of titania in the anatase form, but it cannot be ruled out that a small portion of the sample was in the rutile phase. An upper limit for this can be estimated to be about 10%.

To confirm the Raman results and to perform a more sensitive analysis able to reliably quantify the rutile minority phase, we resorted to powder x-ray diffraction measurements. In Fig. 4, panel A, we report a typical diffractogram obtained from 0.5 mol% Zn-doped titania and subjected to 12 h annealing at 500 ° C. In the same panel we also report the corresponding Rietveld refinement, and the residues in the bottom panel. After the definition of the background, in the refinement we assumed a solid mixture of anatase and rutile phases, whose position of the diffraction peaks is indicated by vertical ticks in the panel. We refined unit cell parameters, and weight fractions of the two phases, as well as peak broadening due to particle size. Results are reported in Table 2. Incidentally, we note the presence of a couple of instrumental artifacts present in all the diffractograms and related to the 2D area detector non-homogeneous efficiency: one at 2 $\theta \sim 30°$ and one appearing as a broad feature extending from 2 $\theta \sim 50°$ to 2 $\theta \sim 53°$ with a tiny sharp spike at 2 $\theta \sim 51.56°$, marked by a black asterisk in the graph.

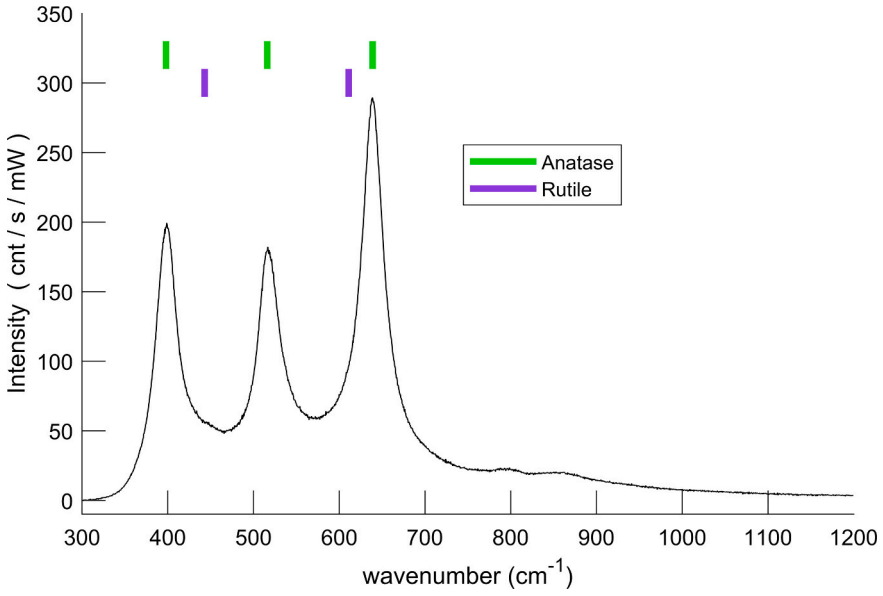

Fig. 3. Raman spectra of TiO_2 NPs powder doped with 4 *mol% Zn*, calcined at 500 ° *C* for 2 h. Vertical bars indicate the position of the Raman peaks of anatase phase (green) and rutile phase (purple), respectively. (For interpretation of the references to colour in this figure legend, the reader is referred to the web version of this article.)

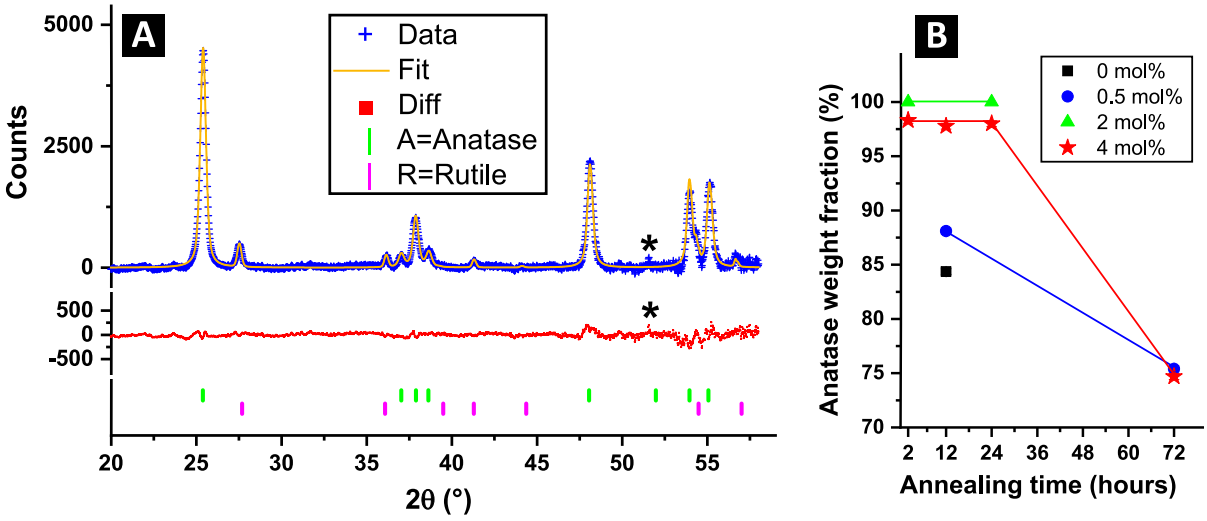

Fig. 4. A) Rietveld refinement (reduced $\chi^2 = 0.174$) of powder diffraction data of 0.5 *mol% Zn*– doped titania nanoparticles after 12 h annealing at 500 ° *C*. Calculated pattern is shown in yellow, while observed data are in blue and residual in red. Purple and green ticks mark the reflection positions of rutile and anatase phases, respectively. The asterisk at $2\theta \sim 51.56°$ marks a spike ascribed to a detector artifact. B) Weight fraction of anatase as a function of Zn-content and of the annealing time at 500 ° *C* based on the Rietveld analysis of XRD data performed. (For interpretation of the references to colour in this figure legend, the reader is referred to the web version of this article.)

Table 2
Polymorphs content, their corresponding cell parameters, and crystallite size obtained by Rietveld refinement of a powder of NPs 0.5 *mol% Zn*-doped titania subjected to 12 h annealing at 500 ° *C*.

	Anatase	Rutile
Space Group	*I41/amd*	*P42/mnm*
Unit cell parameters	$a = 3.78912(21)$ Å	$a = 4.5990(12)$ Å
	$c = 9.5241(5)$ Å	$c = 2.9637(9)$ Å
Crystallite size	38.51(26) *nm*	116(18) *nm* | 14(7) *nm*
Weight fraction	88.1(5)%	11.9(6)%

The results of the Rietveld refinements, as the weight fraction of each polymorph, the corresponding unit cell parameters and crystallite sizes are reported in Table ST1 (SI) for all the samples investigated, spanning Zn doping level up to 4 mol% and annealing time at 500 ° C up to 72 h. The values of the fitted unit cell parameters are in nice agreement with the literature [26]. Comparing the crystalline structures obtained by different Zn doping (0.5 and 4 mol%) after annealing at 500 ° C for 12 and 72 h, we note that the 0.5 mol% Zn doped sample displays the highest stability of unit cell parameters against the temperature.

Panel B of Fig. 4 shows the evolution of the weight fraction of anatase in samples of different Zn doping as a function of annealing time: anatase is always confirmed as the majority phase, accounting for more than 85% of all the Zn doped sample for annealing times up to 24 h. On

the contrary, 72 h of annealing resulted in a decrease of anatase phase to 75%, the remaining 25% being converted to the rutile phase. In two samples we also found a small contamination from titanium (III) chloride, accounting respectively for 1.58% and 0.51% of the mass of the sample. It might arise from incomplete sol-gel reaction. However, given its negligible amount, we do not discuss it further.

At the same time the fitted crystallite sizes are relatively smaller than the NPs size determined by DSL and SEM, suggesting that individual NPs are indeed polycrystalline. We also noted that for the same annealing duration and percentage of Zn, the crystallite size of rutile is generally larger than that of anatase, presumably because of ongoing recrystallization processes. These results regarding the stability of anatase polymorph, and the phase evolution as a function of the thermal treatments are consistent with the literature [9,10], confirming that an appropriate Zn doping may be used to stabilize anatase phase up to higher temperatures and longer times as it could be required for the formation of the solid foam. Incidentally we noted that whenever prolonged annealing times are required, as it could be the case for the stabilization of solid foams, best results were obtained by a slightly higher doping level (2 mol%) than previously reported [6], where optimal stability was achieved at 0.5 mol%, but related to shorter annealing times (ca. 2 h) at the same temperature of 500 ° C.

3.4. Photocatalytic activity measurements

Photocatalysis experiments in water, in analogy with the literature [6], to validate the PCO capability of the NP synthesized by us were performed. Fig. 5 reports data for titania NPs doped with Zn 0.5 mol% and subjected to a thermal treatment of 12 h at 500 ° C. In panel A we report the evolution of the spectrum of RhB as a function of irradiation time. Careful inspection reveals a slight change in the spectral shape as a function of irradiation time: the low wavelength shoulder around 530 nm increases its spectral weight with respect to the main peak around 550 nm (see also Fig. S2 in SI for a detailed analysis of spectral shape). This effect is well-known in the literature [27], and is a signature of photoinduced de-ethylation of RhB. This validates the assumption of PCO activity, as opposed to the possibility of simple physisorption of RhB molecules on the NP surfaces, which on the contrary, would result in a similar decrease of the absorbance peak but not accompanied with the reported spectral change [27].

In panel B of Fig. 5 we compare the decay of the concentration in the presence and absence of NPs (control sample). The absence of decay for the control sample excludes the occurrence of photolysis, indicating the mildness of the oxidizing conditions, which is different of what reported in [6], where photolysis of RhB was responsible of halving its concentration in 60 min, presumably because oxygen was flushed in the sample during the measurement. On the contrary, in the present case even in mild conditions, a sizeable decay of concentration of RhB was detected in the sample with NPs, in which the RhB concentration halves after 120 min of irradiation. It can be therefore concluded that the photocatalytic activity of the NPs is in line with the literature.

3.5. Foam stabilization and formation of solid foams

We investigated the formation of complexes of NPs and CTAB, and their ability to stabilize liquid foams. A schematic representation of the formation of these complexes and their interfacial activity at the air/water interface is shown in Fig. 6, panel A, for increasing surfactant concentrations, from A1 to A4: the optimal surfactant content (A3) lays between the two extremes represented respectively by i) the regime of little surfactant content (panels A1 and A2), in which the NPs are too hydrophilic to effectively stabilize the air/water interface, and by ii) the regime of too high surfactant content (panel A4), in which excess of surfactant might form nanostructures on the particles which make complexes hydrophilic again. Panel B in Fig. 6 reports a typical image of a liquid foam. From time series of such images, we obtained the temporal evolution of foam height, reported in panel C, for different CTAB contents. Panel D (Fig. 6) reports the same data as a function of CTAB content for different given times, indicated in the caption.

Remarkable stability of the foam is obtained in the best conditions, with a foam retaining more than 90% of its volume even after many hours. A broad maximum of stability is found for CTAB content in the range 10 − 100 μmol per gram of nanoparticles. This is consistent with previous findings, demonstrating that the degree of amphiphilicity of the complexes formed by hydrophilic particles, silica and titania, and ionic surfactant CTAB could be finely tuned by varying the content of surfactant [20].

We obtained solid foams by jellification of the liquid fraction, and an example is shown in panel A of Fig. 7. In panel B we report a typical SEM image of the same solid foam, together with a graph of the pore size

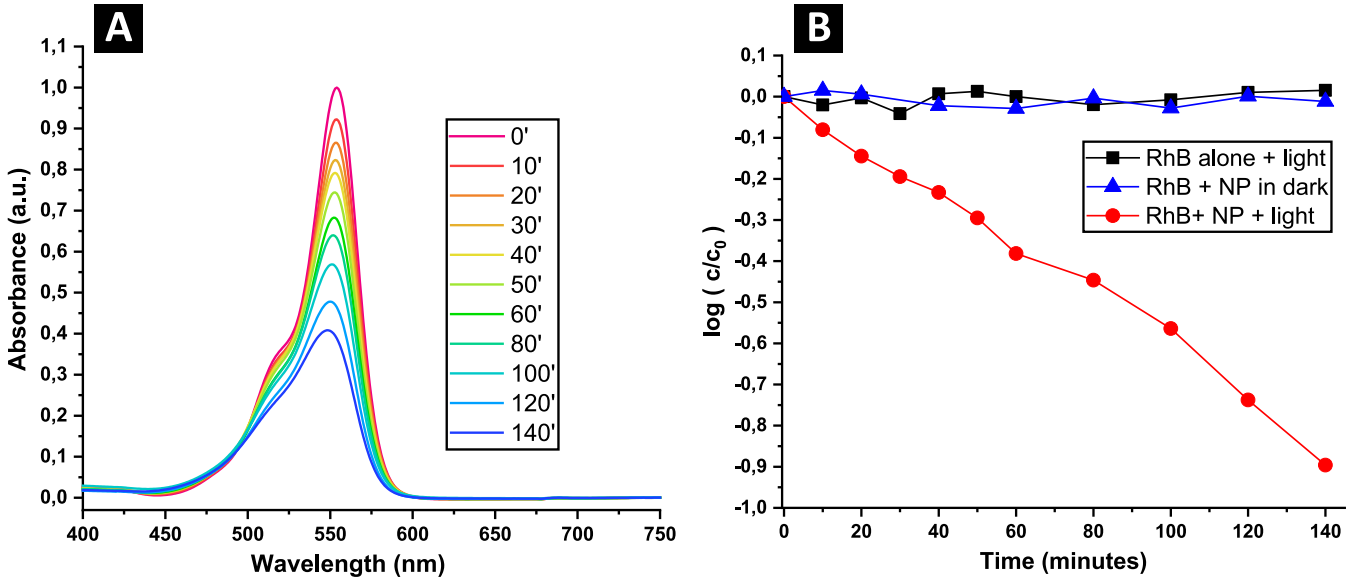

Fig. 5. Quantification of photocatalytic activity of *Zn*-doped titania nanoparticles on Rhodamine B under a solar simulator lamp. A) Rhodamine B solution spectra as a function of irradiation time. B) Time evolution of Rhodamine B concentration during PCO experiments: RhB under illumination but no NP (squares), RhB + NP but no light (triangles), and RhB + NP under illumination (circles).

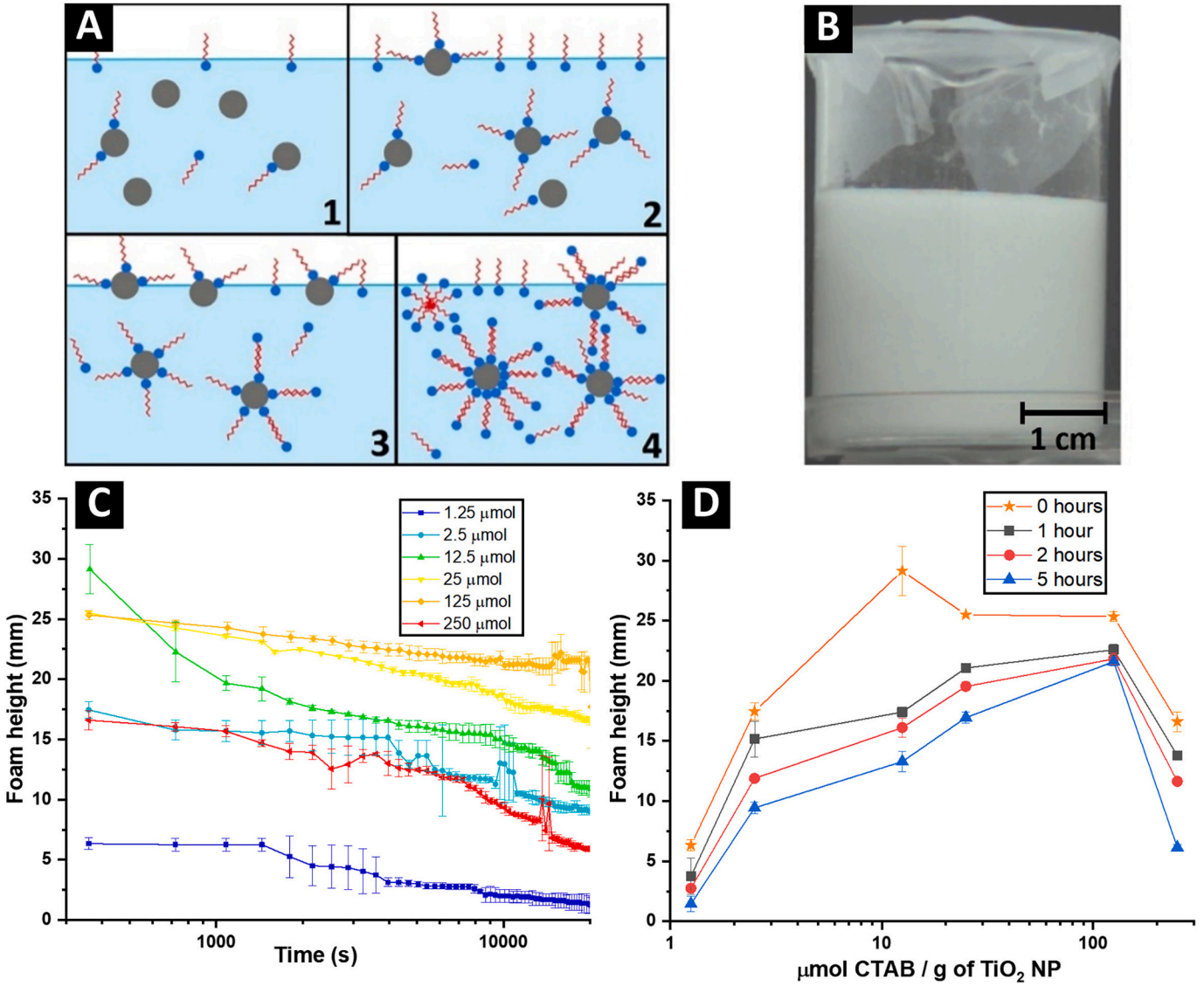

Fig. 6. A) Artist's impression of the mechanism of formation of complexes of NPs with CTAB. Frames 1 to 4 reflect the different scenarios for increasing the amount of CTAB. B) Example of a liquid foam obtained by 125 *µmol* of CTAB per gram of nanoparticles. C) Height of the foams as function of aging, for different amounts of CTAB per gram of nanoparticles (values indicated in the legend). D) Height of the foams at constant aging time (as indicated in the legend) as a function of CTAB content per gram of nanoparticles.

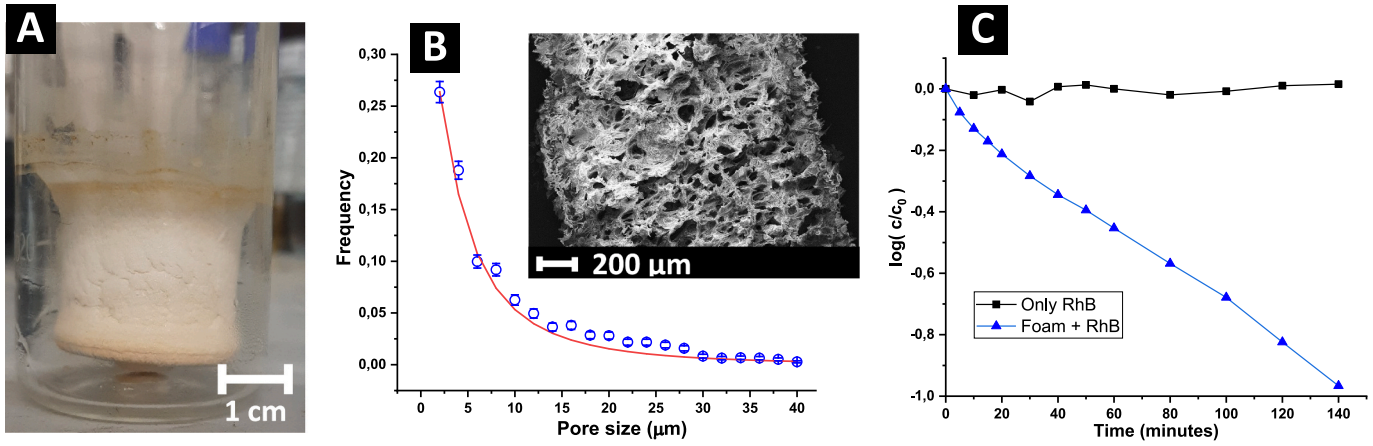

Fig. 7. A) An example of solid foam. B) Pore size distribution (symbols) obtained by processing a set of SEM images (an example of which is shown in the inset). The red line is a phenomenological fit to the lognormal distribution described in the text. C) Photocatalytic activity of the solid foam tested for the oxidation of RhB in water solution. Here, the RhB concentration is reported as a function of irradiation time (blue triangles), where for comparison we report also the control experiment with RhB alone (black squares). (For interpretation of the references to colour in this figure legend, the reader is referred to the web version of this article.)

distribution obtained by a set of images analyzed by the algorithm explained in the Supplementary Information. This distribution can be phenomenologically described by a lognormal distribution (red line in the graph) providing a mean of 9.3 μm and a variance of 283.4 μm^2. The open pore structure of the foam, already evident from the images, is confirmed by the fact that this foam is capable to reversibly adsorbing and desorbing water molecules for up to five times its weight.

The photocatalytic activity of the solid foam was tested in analogy with the test performed on the NPs. The results are shown in panel C of Fig. 7, which reports on a log-scale the decrease of RhB concentration as a function of irradiation time (blue triangles), compared to the control experiment on RhB alone (black squares). UV–vis absorption spectra are reported in Fig. S3 (SI); they show the hallmarks of photoinduced de-ethylation of RhB, in strict analogy to the case of the PCO experiment with the NP suspension. The experiment was repeated in triplicate with analogous results. The observed rate of photocatalytic degradation by the foam slightly exceeds that by the NPs alone. These results demonstrate that the solid foam offers excellent PCO capabilities, extending past works [18–20] in which allumina, silica and carbon soot NPs were employed to form particle-laden interfaces that allowed the stabilization of foams.

One issue to be addressed in the perspective use of a foam PCO filter is the reasonably uniform illumination of the whole foam structure to ensure optimal photoactivation of the catalytic process, a feature not available with the current state-of-the art bulk ceramic photocatalytic filters. Transmission measurements performed on different solid foams allowed to evaluate the penetration depth in the UV–vis range. The values obtained lay in the sub-millimetric to millimetric range and depend on pore size and process parameters. While this is clearly enough to effectively activate PCO (see data in Fig. 7), if longer penetration lengths could be obtained, it would probably allow more efficient PCO. This could be pursued by a two-fold approach: on one side, by realizing foams stabilized by a mixture of titania and silica NPs, thus exploiting the optical properties of the latter, and on the other side by devising foams with a broader pore distribution, thus ensuring more effective penetration of light. In both cases, optical Monte Carlo and ray-tracing simulations [28,29] are well-established techniques that can be employed to model light diffusion in such inhomogeneous media.

4. Conclusions and outlook

In this work we successfully synthesized Zn-doped titania nanoparticles in the range 0.5 to 4 mol% Zn/Ti molar ratio. Their morphology was checked by SEM and DLS, confirming that it consists of primary particles of size around 70 nm, which form clusters. Raman and X-ray diffraction techniques confirmed that - even after annealing at 500 ° C for 24 h- the photocatalytic anatase phase is predominant, accounting for more than 85% in weight. The band gap was determined by Tauc plot of the diffuse reflectivity, and it agrees with the values reported for Zn doped titania. The photocatalytic capability of these NPs was tested by degrading Rhodamine B in a water suspension of 0.5 mol % Zn-doped titania NPs. The results thus obtained are in line with the literature and confirm in principle the applicability of these NPs to form PCO filters. We then exploited surface science concepts to form complexes of NPs and CTAB cationic surfactant, whose interfacial activity was maximized by tuning the NP/surfactant ratio. These complexes were used to stabilize both liquid and solid foams, whose morphology and pore size distribution was characterized by SEM and optical microscopy. We then demonstrated excellent photocatalytic activity of the solid foam in water.

These results pave the way to the development of compact and energy efficient PCO filters made by objects of hierarchical porosity obtained from foams stabilized by photocatalytic NPs. These efficient filters may find applications for air purification in industrial and nosocomial environments as well as in demanding sectors, like aerospace. In fact, for human exploration of space - a sector considered strategic by NASA and ESA agencies – the need for new technologies to prevent and counter the formation and proliferation of pathogens in the air and water is generally recognized as a priority. This need could be satisfied by photocatalytic solid foams.

Authors' contributions

Conceptualization, Methodology and Supervision: CL, with initial inputs from RF and LL.

Nanoparticle synthesis: CM, VM, OD, CL.

DLS and SEM characterizations: CM, VL, OD, VM, CL.

UV–vis characterizations: BaA, CM, VM.

Raman characterizations: OD, CL.

XRD characterizations: PD, VM, CM, CL.

Test of photocatalytic activity: BoA, CM, VM, OD, CL.

Foams formation: CM, VL, VM, SE, CL.

CL wrote the manuscript with help from VM, BoA, BaA, PD, OD.

All the authors commented on the manuscript and approved it.

Declaration of Competing Interest

The authors declare that they have no known competing financial interests or personal relationships that could have appeared to influence the work reported in this paper.

Data availability

Data will be made available on request.

Acknowledgements

Help from Ms. Samantha Saleri, Ms. Maria Concetta Mele, and Mr. Davide Calzetti with some of the NPs synthesis and characterizations is gratefully acknowledged. The authors wish to acknowledge the financial support of the European Space Agency, within the MAP project "Emulsion Dynamics and Droplet Interfaces - EDDI" (ESA Contract n. 4000128643/19/NL/PG).

Appendix A. Supplementary data

Supplementary data to this article can be found online at https://doi.org/10.1016/j.catcom.2022.106527.

References

[1] US EPA, Residential Air Cleaners: A Technical Summary. https://www.epa.gov/sites/default/files/2018-07/documents/residential_air_cleaners_-_a_technical_summary_3rd_edition.pdf, 2018.
[2] Y. Muramoto, M. Kimura, S. Nouda, Development and future of ultraviolet light-emitting diodes: UV-LED will replace the UV lamp, Semicond. Sci. Technol. 29 (2014), 084004, https://doi.org/10.1088/0268-1242/29/8/084004.
[3] T. Luttrell, S. Halpegamage, J. Tao, A. Kramer, E. Sutter, M. Batzill, Why is anatase a better photocatalyst than rutile? - model studies on epitaxial TiO2 films, Sci. Rep. 4 (2015) 1–8, https://doi.org/10.1038/srep04043.
[4] J. Schneider, M. Matsuoka, M. Takeuchi, J. Zhang, Y. Horiuchi, M. Anpo, D. W. Bahnemann, Understanding TiO2photocatalysis: mechanisms and materials, Chem. Rev. 114 (2014) 9919–9986, https://doi.org/10.1021/cr5001892.
[5] D. Reyes-Coronado, G. Rodríguez-Gattorno, M.E. Espinosa-Pesqueira, C. Cab, R. De Coss, G. Oskam, Phase-pure TiO2 nanoparticles: Anatase, brookite and rutile, Nanotechnology. 19 (2008), https://doi.org/10.1088/0957-4484/19/14/145605.
[6] G. Liu, X. Zhang, Y. Xu, X. Niu, L. Zheng, X. Ding, The preparation of Zn2+−doped TiO2 nanoparticles by sol–gel and solid phase reaction methods respectively and their photocatalytic activities, Chemosphere. 59 (2005) 1367–1371, https://doi.org/10.1016/j.chemosphere.2004.11.072.
[7] D.L. Liao, C.A. Badour, B.Q. Liao, Preparation of nanosized TiO2/ZnO composite catalyst and its photocatalytic activity for degradation of methyl orange, J. Photochem. Photobiol. A Chem. 194 (2008) 11–19, https://doi.org/10.1016/j.jphotochem.2007.07.008.
[8] M. Ahamed, M.A.M. Khan, M.J. Akhtar, H.A. Alhadlaq, A. Alshamsan, Ag-doping regulates the cytotoxicity of TiO2 nanoparticles via oxidative stress in human cancer cells, Sci. Rep. 7 (2017) 17662, https://doi.org/10.1038/s41598-017-17559-9.
[9] S. Vargas, R. Arroyo, E. Haro, R. Rodríguez, Effects of cationic dopants on the phase transition temperature of titania prepared by the sol-gel method, J. Mater. Res. 14 (1999) 3932–3937, https://doi.org/10.1557/JMR.1999.0532.
[10] S. Pang, J. Guo Huang, Y. Su, B. Geng, S. Yuan Lei, Y. Ting Huang, C. Lyu, X. Juan Liu, Synthesis and modification of Zn-doped TiO2 nanoparticles for the photocatalytic degradation of tetracycline, Photochem. Photobiol. 92 (2016) 651–657, https://doi.org/10.1111/php.12626.
[11] D. Weaire, S. Hutzler, The Physics of Foams, Oxford University Press, 1999.
[12] I.J. Kim, J.G. Park, Y.H. Han, S.Y. Kim, J.F. Shackelford, Wet foam stability from colloidal suspension to porous ceramics: a review, J. Korean Ceram. Soc. 56 (2019) 211–232, https://doi.org/10.4191/kcers.2019.56.3.02.
[13] J. Zhao, S. Shimai, G. Zhou, J. Zhang, S. Wang, Ceramic foams shaped by oppositely charged dispersant and surfactant, Colloids Surfaces A Physicochem. Eng. Asp. 537 (2018) 210–216, https://doi.org/10.1016/j.colsurfa.2017.10.022.
[14] U.T. Gonzenbach, A.R. Studart, E. Tervoort, L.J. Gauckler, Macroporous ceramics from particle-stabilized wet foams, J. Am. Ceram. Soc. 90 (2007) 16–22, https://doi.org/10.1111/j.1551-2916.2006.01328.x.
[15] C. Chuanuwatanakul, C. Tallon, D.E. Dunstan, G.V. Franks, Controlling the microstructure of ceramic particle stabilized foams: influence of contact angle and particle aggregation, Soft Matter 7 (2011) 11464, https://doi.org/10.1039/c1sm06477k.
[16] S. Ungureanu, M. Birot, H. Deleuze, V. Schmitt, N. Mano, R. Backov, Triple hierarchical micro–meso–macroporous carbonaceous foams bearing highly monodisperse macroporosity, Carbon N. Y. 91 (2015) 311–320, https://doi.org/10.1016/j.carbon.2015.04.092.
[17] D. Zabiegaj, M.T. Buscaglia, D. Giuranno, L. Liggieri, F. Ravera, Activated carbon monoliths from particle stabilized foams, Microporous Mesoporous Mater. 239 (2017) 45–53, https://doi.org/10.1016/j.micromeso.2016.09.046.
[18] D. Zabiegaj, E. Santini, M. Ferrari, L. Liggieri, F. Ravera, Carbon based porous materials from particle stabilized wet foams, Colloids Surfaces A Physicochem. Eng. Asp. 473 (2015) 24–31, https://doi.org/10.1016/j.colsurfa.2015.02.031.
[19] D. Zabiegaj, E. Santini, E. Guzmán, M. Ferrari, L. Liggieri, V. Buscaglia, M. T. Buscaglia, G. Battilana, F. Ravera, Nanoparticle laden interfacial layers and application to foams and solid foams, Colloids Surfaces A Physicochem. Eng. Asp. 438 (2013) 132–140, https://doi.org/10.1016/j.colsurfa.2013.02.046.
[20] S. Llamas, A. Ponce Torres, L. Liggieri, E. Santini, F. Ravera, Surface properties of binary TiO2 - SiO2 nanoparticle dispersions relevant for foams stabilization, Colloids Surfaces A Physicochem. Eng. Asp. 575 (2019) 299–309, https://doi.org/10.1016/j.colsurfa.2019.05.023.
[21] F. Chabert, D.E. Dunstan, G.V. Franks, Cross-linked polyvinyl alcohol as a binder for gelcasting and green machining, J. Am. Ceram. Soc. 91 (2008) 3138–3146, https://doi.org/10.1111/j.1551-2916.2008.02534.x.
[22] B.H. Toby, R.B. Von Dreele, GSAS-II: the genesis of a modern open-source all purpose crystallography software package, J. Appl. Crystallogr. 46 (2013) 544–549, https://doi.org/10.1107/S0021889813003531.
[23] R. López, R. Gómez, Band-gap energy estimation from diffuse reflectance measurements on sol–gel and commercial TiO2: a comparative study, J. Sol-Gel Sci. Technol. 61 (2012) 1–7, https://doi.org/10.1007/s10971-011-2582-9.
[24] J. Pascual, J. Camassel, H. Mathieu, Fine structure in the intrinsic absorption edge of TiO2, Phys. Rev. B 18 (1978) 5606–5614, https://doi.org/10.1103/PhysRevB.18.5606.
[25] L. Miao, S. Tanemura, H. Watanabe, Y. Mori, K. Kaneko, S. Toh, The improvement of optical reactivity for TiO2 thin films by N2–H2 plasma surface-treatment, J. Cryst. Growth 260 (2004) 118–124, https://doi.org/10.1016/j.jcrysgro.2003.08.010.
[26] V.R. Akshay, B. Arun, S. Dash, A.K. Patra, G. Mandal, G.R. Mutta, A. Chanda, M. Vasundhara, Defect mediated mechanism in undoped, Cu and Zn-doped TiO 2 nanocrystals for tailoring the band gap and magnetic properties, RSC Adv. 8 (2018) 41994–42008, https://doi.org/10.1039/c8ra07287f.
[27] T. Wu, G. Liu, J. Zhao, H. Hidaka, N. Serpone, Photoassisted degradation of dye pollutants. V. Self-photosensitized oxidative transformation of rhodamine B under visible light irradiation in aqueous TiO2 dispersions, J. Phys. Chem. B 102 (1998) 5845–5851, https://doi.org/10.1021/jp980922c.
[28] F.F.M. de Mul, Monte-Carlo simulations of Light scattering in turbid media, in: Handb. Coherent-Domain Opt. Methods, Springer New York, New York, NY, 2013, pp. 593–661, https://doi.org/10.1007/978-1-4614-5176-1_15.
[29] V. Lorusso, D. Orsi, F. Salerni, L. Liggieri, F. Ravera, R. McMillin, J. Ferri, L. Cristofolini, Recent developments in emulsion characterization: diffusing wave spectroscopy beyond average values, Adv. Colloid Interf. Sci. 288 (2021), 102341, https://doi.org/10.1016/j.cis.2020.102341.